

## A MODEL FOR HARD X-RAY EMISSION FROM THE TOP OF FLARING LOOPS

L. FLETCHER<sup>1</sup>

Solar System Division, ESA Space Science Department, ESTEC, Postbus 299, 2200 AG Noordwijk, The Netherlands

AND

P. C. H. MARTENS

Solar System Division, ESA Space Science Department at Goddard Space Flight Center, Greenbelt, MD 20771

Received 1997 July 11; accepted 1998 April 22

### ABSTRACT

The frequent occurrence of hard X-ray emission from the top of flaring loops was one of the discoveries by the Hard X-Ray Telescope on board the Japanese *Yohkoh* satellite. In this paper we take a flare current-sheet geometry and show how the combined effect of magnetic field convergence and pitch-angle scattering of nonthermal electrons injected at the top of the loop results in the generation of a looptop source with properties akin to those observed by *Yohkoh*. We demonstrate that a looptop source can be produced in both impulsive and gradual phase loops. We further present a possible mechanism for the generation of high-temperature “ridges” in the loop legs.

*Subject headings:* Sun: corona — Sun: flares — Sun: X-rays, gamma rays

### 1. INTRODUCTION

The appearance of well-resolved, impulsive hard X-ray-emitting sources at the top of loops in limb flares was one of the surprising observational results from the Hard X-Ray Telescope (HXT) on board the Japanese *Yohkoh* satellite and one that has caused a flurry of activity amongst solar flare modelers. Hard X-ray (HXR) sources away from the limb during flares have been reported earlier from observations with the *Solar Maximum Mission* (SMM; Simnett & Strong 1984) and *Hinotori* (Takakura et al. 1987), but their frequency and close spatial coincidence with flare loops is a major result from *Yohkoh*.

Masuda (1994) and Masuda et al. (1995) reported that in the flare of 1992 January 13 (the “Masuda” flare), HXR looptop sources occur at the onset of the impulsive phase of the flare, that they vary rapidly on timescales less than a minute, and that the spectrum of the sources is only slightly softer than those of the footpoint sources. Later in the flare another looptop HXR source appears, which has a more gradual time dependence and a softer spectrum. Masuda et al. (1994) proposed that the looptop sources observed for several limb flares were due to thermal bremsstrahlung emission of a superhot plasma (around  $2 \times 10^8$  K) located above closed field lines and resulting from shock heating, where the cooling flow from an overlying reconnection region meets dense loop plasma. Electrons from this superhot blob of plasma, and also possibly from the acceleration region itself, would then stream down the legs of the loop and cause HXR emission from the loop footpoints, as is also seen in the observations and as predicted by the standard thick-target solar flare model.

Recently, Alexander & Metcalf (1997) presented a careful “Pixon” reanalysis of the “Masuda” event, confirming the initial impulsive behavior of the looptop source in the HXT M1 and M2 channels. They further conclude that the (limited) spectral information on the impulsive looptop source is inconsistent with thermal emission from an isothermal plasma. Hudson & Ryan (1995) also argue that the

impulsive looptop source cannot be thermal, because the thermalization timescale for plasma with the inferred density and temperature of the looptop source is longer than the observed timescale of variations.

Fletcher (1995) proposed that the looptop and footpoint sources were both nonthermal in origin and generated by the same population of particles, with enhanced emission at the top of loops due to initially high pitch-angle beam particles orbiting the field near their site of injection before being scattered into directions along the loop. Emission was found for loop densities on the order of  $n = 3 \times 10^{10} \text{ cm}^{-3}$  and above. Because they are scattered into the forward direction and start to stream down the field lines, flux conservation dictates that the number density of beam electrons, and thus the bremsstrahlung emission, decreases away from the site of acceleration. At the chromosphere the increase in local density leads to the bremsstrahlung yield increasing once more, giving the standard footpoint sources. Although the looptop region does not have the high target density that we normally associate with thick-target behavior, the electrons still lose a large fraction of their energy while orbiting the field at the looptop (Coulomb scattering time approximately equal to Coulomb energy loss time). This leads to a quasi-thick spectrum. The footpoint sources show a harder, thick target spectrum. The HXR spectral index for both the looptop and the footpoint increases as photon energy increases.

Wheatland & Melrose (1995) also proposed that the looptop sources are nonthermal in origin. Their model has a loop target with a dense region at the top of the loop (as is often inferred from *Yohkoh* soft X-ray (SXR) observations, although not from the same flares as those in which HXR looptop sources are seen) plus less dense loop legs and the normal dense chromosphere. This resulted in a “thick-thin-thick” target in which a large fraction of the collisional loss of low-energy particles is in the looptop region, while the higher energy particles precipitate to the footpoints. A looptop source was found for looptop densities of  $\sim 10^{12} \text{ cm}^{-3}$ . Such a model results naturally in a spectral break in both looptop and footpoint source spectra, the position of which is determined chiefly by the total column at the top of the loop: the break occurs at the electron energy ( $\sim$  photon

<sup>1</sup> Current address: Lockheed-Martin Solar and Astrophysics Laboratory, Organization H1-12, Building 252, 3251 Hanover Street, Palo Alto, CA 94304.

energy) below which the looptop is a completely thick target.

Holman (1996) models the emission of nonthermal HXR radiation from the cusp of a magnetic loop structure, such as that proposed by Masuda et al. (1995), but with a semi-circular form. The cusp is the structure connecting the bulk of the loop to the reconnection region. In that work a constant loop density is used, and a looptop source at 30 keV is generated in the cusp structure when the loop density is over  $10^{11} \text{ cm}^{-3}$ . The source appears because the electrons with energy at injection of 30 keV, which also form the bulk of the power-law-injected spectrum, lose most of their energy collisionally and produce HXR bremsstrahlung radiation in the cusp structure. The remainder of the electrons then generate HXR radiation when they reach the dense footpoint. This model, by the same type of argument as is given by Wheatland and Melrose, can successfully account for the spectral behavior shown by the “Masuda” flare.

The work described above concentrates on the scattering and energy loss of beam particles by the microscopic plasma processes at work. They all require in general high particle number densities to generate observable looptop sources—up to  $10^{12} \text{ cm}^{-3}$  at the source site. Although Doschek (1994) has reported a flare loop density of  $1.2 \times 10^{12} \text{ cm}^{-3}$  during the rise phase of a flare, more usual SXR loop densities are a few times  $10^{10} \text{ cm}^{-3}$ , while above the SXR loop, where the HXR source is situated, densities of  $\sim 10^9 \text{ cm}^{-3}$  are inferred (see § 5).

In this article we consider the separate effect of having a magnetic “bottle” at the looptop. Magnetic bottling was included in the Fletcher (1995) calculation, but the convergence only occurred in the footpoint field and had little effect on the looptop source; the coronal part of the loop was uniform, in common with the Wheatland & Melrose (1995) and Holman (1996) work. However, Alexander & Metcalf’s (1997) analysis leads them to conclude that the most likely particle distribution causing both the impulsive looptop and footpoint is partially trapped in the coronal portion of the loop, having a power-law distribution with cutoff at  $\sim 19 \text{ keV}$ .

## 2. THE MAGNETIC FIELD MODEL

The magnetic field environment we use is that of a Syrovatskii-type current sheet (Syrovatskii 1971). Such a current sheet is a component of the Martens & Kuin (1989) flare model. A plot of sample field lines around the current sheet is shown in Figure 1.

The magnetic topology modeled analytically in the Martens & Kuin model is that of the “standard” Carmichael-Sturrock-Hirayama-Kopp and Pneumann scenario (for references, see Martens & Kuin 1989) for two-ribbon flares, in which a filament erupts and field lines reconnect in a current sheet below it. High-energy electrons and protons, generated by direct electric field acceleration (e.g., Litvinenko 1996), are injected from the reconnection site into a postflare arcade of loops forming directly below it. The footpoints of the loops in the arcade form the H $\alpha$  ribbons.

Although the Martens & Kuin model has a more complex field—composed not only of that of the current sheet, but also fields associated with the overlying filament and a background field from photospheric sources—the sheet current dominates the field near the sheet and is ade-

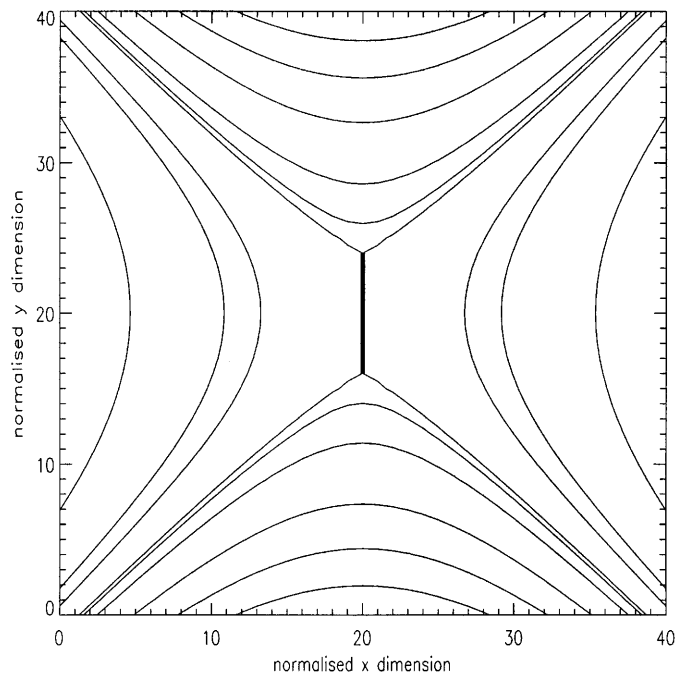


FIG. 1.—Sample field lines plotted for a Syrovatskii-type current sheet with  $b = 0.2$ . In the present model we are concerned with the evolution of electrons that are injected at the top of the field lines below the current sheet.

quate to show the effects of magnetic trapping, which is the purpose of this work. From Figure 1 it can be seen that the distance between field lines is highest directly under the current sheet and decreases as one follows any given field line away from the sheet region. Hence it follows from flux conservation that the field strength along a given field line is minimal at the looptop. We think that particles may be effectively trapped in this magnetic bottle and that a looptop source can originate from bremsstrahlung radiation of electrons confined by the field in this region.

Note that although we have chosen one specific field model, we expect that our present conclusions will hold for any flare field geometry in which the field strength is smallest near the top of loops, as is the case for every geometry involving magnetic neutral points or sheets just above the postflare arcade. The looptop HXR source then provides indirect support for flare models involving magnetic reconnection.

The vector potential associated with the Syrovatskii current sheet is

$$A(x, y) = \text{Re} \left[ \frac{B_0}{2} \left\{ z^2 - z\sqrt{z^2 - b^2} + b^2 \ln [z^2 + \sqrt{z^2 - b^2}] \right\} \right], \quad (1)$$

where  $z = x + iy$ ,  $x$  and  $y$  are the offsets from the center of the current sheet, and  $b$  is the length of the current sheet, in normalized units. After a little reduction,  $B(x, y)$  can also be written in an analytic form:

$$B^2(x, y) = B_0^2 [(x^2 + y^2)^2 + 2b^2(x^2 - y^2) + b^4]^{1/2}. \quad (2)$$

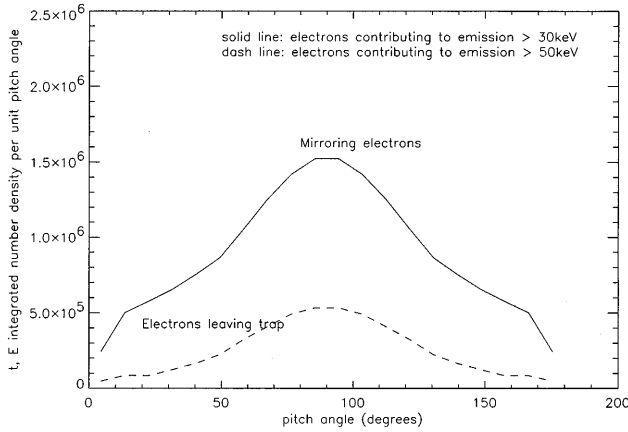


FIG. 2.—Pitch-angle distribution of electrons in the looptop region ( $x = 0-5 \times 10^8$  cm,  $y = 1.3-1.8 \times 10^9$  cm, at energies  $> 30$  keV [solid line] and  $> 50$  keV [dashed line]). The particle number is the time-integrated number of test particles recorded in the simulation.

The parameter  $b$  is the only free length parameter in the field model, and when using it as the global field for the modeling of electron transport, all other dimensions are scaled to this. To fix the field values we use a typical foot-point field at the corners of the structures, which then defines the field throughout the region. There is no restriction in the field model on the local density structure in the field: we choose this to be constant, in the coronal part of the loop, to make clear the effect of magnetic trapping/particle scattering processes rather than changes resulting from an inhomogeneous density structure.

Support for the field geometry in our model can be found in the frequently observed cusp structure of flaring plasma in soft X-ray telescope (SXT) observations (for example, see the beautiful series of images for the 1992 February 20–21 flare in Tsuneta et al. 1992). Since the SXR-emitting plasma maps the magnetic field lines, this field shape is consistent with that expected near a current-sheet geometry.

One would hope also to see this structure reflected in the HXR source (as we calculate in this paper), but the expected looptop source sizes combined with the limited HXT resolution make this unlikely. For instance, consider the observations of the 1992 January 13 flare, described by Masuda et al. (1994). In their Figure 3 we measure a horizontal cross section for the looptop source in the M1 band (24–35 keV) of  $17''$  and a vertical one of about  $9''$ . These correspond to 12,600 and 6500 km on the Sun. These numbers, and in particular the 2 to 1 ratio for horizontal to vertical extent of the HXR looptop source, agree rather well with our numerical results shown in Figure 2, for the comparable 20–30 keV energy range.

There is no indication of a cusp shape in the Masuda et al. (1994) figure, which should come as no surprise, given the experimentally determined HXT angular resolution of  $\sim 5''$  (Kosugi et al. 1991) and the tendency of the maximum entropy method for image reconstruction to smooth out large gradients. Moreover, inspection of our Figures 5 and 6 for the model results on HXR emission contours also only reveals a cusplike structure in the weakest part of the low-energy source.

Given the above, it almost comes as a surprise that in the 1992 Oct 4 flare (Masuda et al. 1994, their Fig. 6) one

actually finds a possible instance of a cusped HXR source shape in the M1 band.

### 3. THE SIMULATION

As in Fletcher (1995, 1996), we will use a stochastic simulation to model the transport of electrons in the magnetic field structure, calculating the effects of magnetic mirroring and Coulomb scattering/energy loss on the evolution of the electron distribution. Ample description of this method can be found in, for example, MacKinnon & Craig (1991), Fletcher (1995, 1996), and we will say nothing about it here, save that it is a Monte Carlo type of simulation in which the orbits of test particles under the influence of their environment are followed by time-stepping the stochastic differential equations for individual particle orbits, using a stochastic term to describe the diffusion process. It is a method that has proved to be reliable when tested against analytic solutions of the Fokker-Planck evolution equation. It is used here since it allows one a great deal of freedom in choosing initial conditions and boundary conditions for the situation to be studied, permitting the calculation of the electron distribution function evolution in a much greater range of field geometries than is analytically treatable. This makes it ideal for the type of problem studied here, where geometry is crucial.

The Fokker-Planck equation, which will be (numerically) solved in this case is

$$\frac{\partial f}{\partial t} + \mu v \frac{\partial f}{\partial S} - \frac{4\pi e^4 \Lambda n}{m_e} \frac{\partial}{\partial E} \left( \frac{f}{v} \right) - \frac{v}{2} \frac{\partial}{\partial \mu} \left[ (1 - \mu^2) \frac{d \ln B}{dS} f \right] - \frac{4\pi e^4 \Lambda n}{m_e^2 v^3} \frac{\partial}{\partial \mu} \left[ (1 - \mu^2) \frac{\partial f}{\partial \mu} \right] = 0. \quad (3)$$

Here  $f = f(x, y, v, \mu, t)$  is the distribution function of test electrons, and is a function of the two spatial dimensions, electron pitch-angle cosine  $\mu$ , speed  $v$  and time.  $S = S(x, y, x_0, y_0)$  is the displacement of a particle along a field line from its point of injection ( $x_0, y_0$ ). The electron rest mass and charge are given by  $m_e$  and  $e$ , and  $\Lambda$  is the Coulomb logarithm (see Emslie 1978). We assume that the background is a fully ionized hydrogen plasma of density  $n$ . Equation (3) differs from that studied in Fletcher (1995) in that the magnetic field convergence is a function not only of a test particle's distance from its injection position, but also of the field line to which it is attached (note that we are neglecting cross field drift). What this means in practical terms is that the field conditions for each particle are different and depend on the position at which it is injected, which leads to a considerable increase in the simulation run time compared to the simple field case of Fletcher (1995).

If we look at the equation for the change of particle pitch-angle cosine ( $\mu$ ) due to magnetic field convergence, viz.,

$$\delta \mu = -\frac{v}{2} (1 - \mu^2) \frac{d \ln B(x, y)}{dS(x, y)} dt, \quad (4)$$

we see that this requires the gradient of the field strength along a given field line as a function of position ( $x, y$ ). Although in the case studied there is a simple analytic form for the field strength as a function of ( $x, y$ ), in general there is no tidy analytic expression for the equations of the field lines themselves [ $S(x, y, x_0, y_0)$ ], making it impossible to calculate analytically the field gradient as a function of position along a given field line. In the simulation we resort to a

look-up table of  $(x, y)$  values on a given field line, which has been calculated by tracing the contours of the vector potential associated with the current-sheet geometry. When a particle is started off on a field line at  $(x_0, y_0)$ , the look-up table for this field line is generated and its further motion is at all times confined to the set of line segments defined by this. A change in  $S$ , an electron's position along the field line, must be converted to changes in  $x$  and  $y$  to allow calculation of the magnitude of the magnetic field at the subsequent particle position, and so on.

We have calculated the development of the conserved quantity  $p_{\perp}^2/B$ , the first adiabatic invariant, in a simulation without scattering, and we find that in a simulation lasting 0.5 s (appropriate for a 30 keV electron in an ambient density of a few times  $10^{10} \text{ cm}^{-3}$ ) the first adiabatic invariant is conserved to better than 0.1% for a time step of  $10^{-4}$  s and 150 grid points in the field calculation. In a simulation lasting 5 s, (appropriate for a 30 keV electron in a density of a few times  $10^9 \text{ cm}^{-3}$ ) it is conserved to better than 1%. The accuracy to which the first adiabatic invariant is conserved is dependent on both the time step chosen and the spacing of the calculation grid (as further simulations have shown, with higher resolution giving more exact conservation), and we consider that in the trade-off between long run times/computer memory capacity and high computational accuracy, we have reached a reasonable balance with the above parameters.

### 3.1. Initial Conditions

Although we improve upon the Fletcher (1995) model for the process by the inclusion of a more realistic field model that allows us to study the effect of bottling at the looptop, we are as yet still not concerned with modeling the acceleration process itself or the resulting parameters of the injected electron spectrum. We assume, in line with previous studies, that the injected spectrum has a power-law distribution in flux,  $F(E) = F_0 E^{-\delta}$ , and choose  $\delta = 3$ . The low-energy cutoff to the electron spectrum is at  $E = 15 \text{ keV}$ , thus below the minimum photon energy for which we calculate the source appearance. The angular distribution of injected electrons we can vary at will. The results presented in § 4 are for a distribution of electrons injected uniformly over pitch angle,  $f(\theta) = \text{const}$ , in the forward hemisphere, i.e., equal numbers of electrons per bin in pitch angle in the simulations. Note that this is *not* equivalent to an isotropic distribution, this latter being one which is injected uniformly over solid angle  $d\Omega = \sin \theta d\theta d\phi$ , with  $\phi$  the azimuthal angle. In solid angle our distribution is  $f(\Omega) = \text{const}/2\pi \sin \theta$ , which is a beamed distribution. Any singularity at the beam axis  $\theta = 0$  is avoided by the discrete nature of the simulation. The injected beam in three dimensions has a  $1/e$  width of  $15^\circ$  found by examining the distribution in solid angle, as a function of  $\theta$  and identifying the first angular bin containing a fraction less than  $1/e$  of the central ( $\theta = 0$ ) bin. This is consistent with the typical mean pitch-angle distributions found from the reconnecting current sheet models of Litvinenko (1996) and Martens (1988). These models predict that particles entering the sheet with the mean thermal velocity, which we assume to correspond to a temperature of  $2\text{--}3 \times 10^6 \text{ K}$ , are ejected almost parallel to the reconnecting field at velocity  $v_{ej}$ , the pitch angle being given by  $\tan^{-1} v_{\text{thermal}}/v_{ej}$ . The maximum value of  $v_{ej}$  in the Litvinenko model depends on the structure of the magnetic field within the current sheet, particu-

larly the value  $B_{\text{long}}$  of the longitudinal component of the magnetic field (in our geometry, the component out of the  $x$ - $y$  plane), but for reasonable values of this component, typical average pitch angles are  $4^\circ$  for  $B_{\text{long}} = 100 \text{ G}$  or  $10^\circ$  for  $B_{\text{long}} = 10 \text{ G}$ .

Reconnection and particle acceleration take place in the current sheet and result in the injection of electrons and protons onto those field lines that pass through the sheet as they reconnect to form the postflare arcade. This is a dynamic process; new loops are formed all the time in the rising current sheet. The actual reconnection takes place at the center point of the sheet in any current sheet model that we know of (see Priest 1981). In the collisionless reconnection and acceleration model developed for the solar flare setting by Martens (1988), Martens & Young (1990), and Litvinenko (1996), particles are ejected sideways from the sheet and beamed along the field direction, and they travel along the field lines. We note that in the bottom half of the current sheet (which we model in this paper), the field lines emanating from the sheet connect to the solar surface. Hence the accelerated particles enter into newly closed field lines, the so-called postflare loops.

Since the rise of the current sheet ( $10\text{--}100 \text{ km s}^{-1}$ ; Martens & Kuin 1989) is slow compared to the particle beam propagation along the loop ( $>1 \text{ s}$  for the slowest particles), it is reasonable to use a static magnetic field. However, we have not been able to find a self-consistent and sufficiently simple analytic model of a reconnecting current sheet for use in our simulations. The Syrovatskii model described in the previous section is our best approximation: it has a discontinuity in the field line mapping through the sheet, implying that no field lines actually pass through the sheet. To compensate for this deficiency of the model, we inject particles at the top of the field lines just below the current sheet. The vertical extent of the injection region is about the same as the vertical extent of the bottom half of the current sheet, 0.16 and 0.2 in dimensionless units (defined by the height of the center of the current sheet above the solar surface). With this choice the injection region occupies the top 20% of the postflare arcade in both cases.

It is instructive to consider here magnetic field evolution in the current sheet in a little more depth. In the simulations described below, we choose the length unit equal to  $1.6 \times 10^9 \text{ cm}$ . Hence the vertical extent of the current sheet is  $3.2 \times 10^8 \text{ cm}$ . For a coronal density of about  $4 \times 10^9 \text{ cm}^{-3}$  in preflare loops (see the justification in § 5) and a magnetic field strength of 100 G, one finds an Alfvén velocity of  $5 \times 10^8 \text{ cm s}^{-1}$ . The field lines leave the current sheet with a downward velocity of  $V_A$  and have no downward velocity at the moment of reconnection. Assuming an average velocity of  $V_A/2$ , we find that a field line spends 1 to 2 s in the current sheet, which therefore must be equal to the duration of the acceleration pulse along the field line. (Coincidentally, this duration is similar to the timescale of the simulations presented below.)

### 3.2. Hard X-Ray Emission

The numerical simulations allow one to build up a distribution  $f(x, y, E, t)$  of electrons (this is a number density rather than a flux). From this one calculates the HXR emission by convolving with the emission cross section and electron velocity (to change density into flux). The relevant equation, assuming bremsstrahlung emission by electrons

in a completely ionized hydrogen plasma, is

$$I(x, y, \epsilon, t) = \int_{\epsilon}^{\infty} f(x, y, E, t) n(x, y, t) v(E) \sigma(\epsilon, E) dE, \quad (5)$$

where  $n(x, y, t)$  is the target density (although we do not consider time dependence here),  $\epsilon$  is the photon energy, and  $\sigma(\epsilon, E)$  is the nonrelativistic Bethe-Heitler cross section. Although we are dealing here with mildly relativistic electrons, the nonrelativistic cross section is accurate to  $\sim 20\%$  at the electron and photon energies of interest. Higher order, relativistic corrections are available (Haug 1997), but for comparison we retain the cross sections used in earlier work. It is assumed that the loop structure is being viewed side-on, and there is no account taken of possible variations in structure dimension along the line-of-sight. Likewise, no account is taken of anisotropies in the radiation pattern of bremsstrahlung radiation. Bremsstrahlung emission of relativistic electrons is beamed along the instantaneous direction of travel of the electron in a cone of half-angle  $\sim \sin^{-1}(1/\gamma)$ . At the nonrelativistic electron energies under consideration, this beaming cone will be very wide, but radiation is not isotropic. Directivity effects should therefore be discussed.

Although the numerical simulation does demand that the electron pitch angles are correctly calculated (so that position and energy evolution proceeds correctly), the final pitch-angle distribution is not used to calculate the HXR emission pattern, although evidently the simulation provides the opportunity to do this. Instead, we fold the angle-averaged cross section with the angle-integrated electron number density to calculate local intensities. This is equivalent to assuming both radiation pattern and electron distribution to be isotropic. Some justification for doing this is as follows, based a priori on the forms of the angular dependence in the particle distributions used in the calculation of Figures 5 and 6 in the next section.

In the footpoints the distribution is isotropized by collisions anyway, and angle-dependent effects are smoothed out. Confirming this, Brown (1972) concluded that, especially in flares near the limb, directivity effects can be neglected in the analysis of spectra up to 150 keV generated by scattering beams in chromospheric targets.

In the looptop the angular distribution is not isotropic and the situation must be approached with more caution. The pitch-angle distribution (Figs. 2 and 3) of electrons above 30 keV and above 50 keV, which contribute to HXR emission in the HXT M1 and M2 bands, shows that most have high pitch angles. Plotting the whole (all electrons above 15 keV) distribution differential in solid angle, i.e., dividing by  $\sin \theta$ , where  $\theta$  is the pitch angle, shows that the distribution function has a more-or-less isotropic part, corresponding to particles mirroring and scattering in the trap, and a bidirectional beam component, corresponding to the electrons which escape the trap (Fig. 4). For the isotropic component we can again use the angle-averaged cross section and neglect directivity effects on the intensity and spectrum with some confidence.

For the beam component we must appeal to other arguments. Recall the geometry of the loops in which the looptop HXR sources are observed. They are all limb flares, and in most cases (see Masuda 1995), particularly in the prototypical Masuda event of 1992 January 13, both footpoints are visible on the limb. The loops must therefore be oriented in a plane more or less perpendicular to the line of

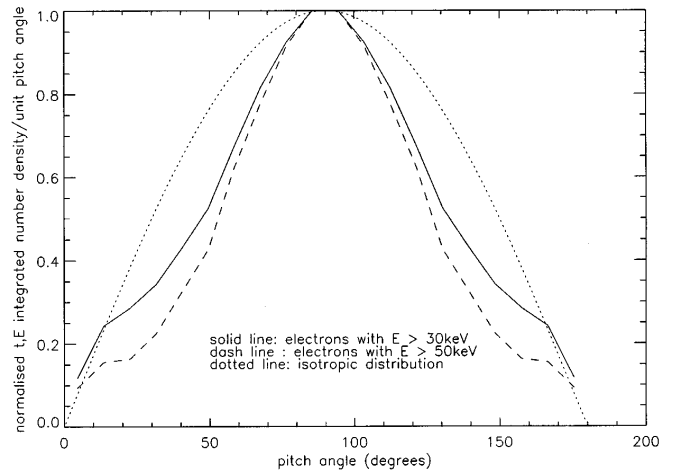


FIG. 3.—Pitch-angle distribution of electrons in the looptop region, at energies  $> 30$  keV (solid line) and  $> 50$  keV (dashed line), normalized to the maximum number in each energy range. The dotted line is the isotropic [ $f(\theta) = \sin \theta$ ] distribution.

sight, meaning that the beam axis of symmetry is also in a plane perpendicular to the line-of-sight. We are thus observing the emission at  $\sim 90^\circ$  to the beam axis. Elwert & Haug (1972) studied the *noncollisional* emission from electrons spiraling in a magnetic field and found that emission by an electron distribution of spectral index 3, at photon energy 50 keV, is more or less isotropic for high pitch-angle particles; i.e., the bulk of our looptop distribution, and moreover, the bremsstrahlung yields at a viewing angle of  $90^\circ$  are more or less independent of the pitch angle of the radiating electron (see their Figs. 3 and 4). Note that Elwert & Haug (1972) used a cut-off energy of 2.5 keV rather than the value of 15 keV that we use, but because only electrons of energy  $\geq 30$  keV contribute to the parts of the spectrum in which we are interested, this is not a problem. Petrosian (1973) extended this to consider the directivity of HXR emission from beam distributions undergoing collisional losses,

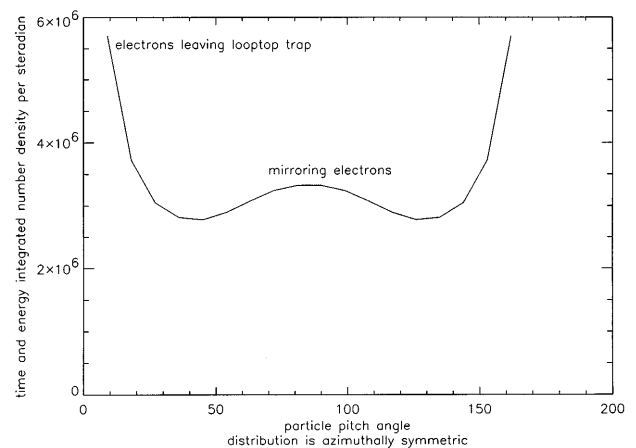


FIG. 4.—Solid-angle distribution of all electrons in the looptop region, showing the almost isotropic mirroring component at pitch angles of  $\sim 90^\circ$  and the beam distributions leaving the looptop in opposite directions. The particle number is the time-integrated number of test particles recorded in the simulation, divided by  $\sin \theta$ , where  $\theta$  is the pitch angle. Note that this figure includes all electrons, from 15 keV upward, unlike the distributions in Fig. 2, which show only the higher energy parts of the total distribution.

showing that for a beam propagating perpendicular to the line-of-sight, the angle-dependent bremsstrahlung intensity is almost equal to the angle-averaged bremsstrahlung intensity (the ratio varies between  $\sim 0.7$  and  $1.2$ , depending on photon energy) for photon energies up to  $\sim 50$  keV and beam input spectra with power-law indices between 3 and 5. He further showed that the variation with viewing angle of the 20–70 keV photon spectral index under these conditions was minimal. Note that we are not concerned, as Petrosian was, with a strictly unidirectional beam: rather, with a beamed distribution. However, the strict beam provides the least isotropic conditions and thus the worst case for differences between angle-averaged and angle-dependent yields. So a more isotropic distribution should, as long it has an axis of azimuthal symmetry perpendicular to the line of sight, show no greater and probably smaller differences in the ratio of angle-dependent to angle-averaged emission.

So, from previous work it appears that, because the geometry is such that we view the emission at right angles to the beam axis of symmetry, both absolute intensity and spectrum of the emission should be adequately represented by values calculated with angle-averaged formulae. But this does not provide a general justification for the neglect of directional effects in the calculation of HXR spectra: it is specific to this geometry. Further investigations into directional effects, such as how looptop sources might appear at different locations on the disk, should prove interesting.

#### 4. RESULTS OF THE SIMULATIONS

##### 4.1. Comparison between Trapping and Nontrapping Cases

To get some idea of the changes in the looptop source introduced by having a convergent magnetic field, we have chosen the simulation parameters to be the same as the first simulations by Fletcher (1995) but with the convergent

coronal field geometry. The conditions, in addition to those described above, are as follows:  $n_e = 3 \times 10^{10} \text{ cm}^{-3}$  (coronal plasma; completely ionized hydrogen assumed), loop half-length in corona =  $2.2 \times 10^9 \text{ cm}$ , extent of chromosphere =  $2 \times 10^8 \text{ cm}$ , and density in the chromosphere is matched to that of the corona and increases exponentially downward, with a maximum value of  $9.23 \times 10^{16} \text{ cm}^{-3}$ . The magnetic field strength at the footpoint ( $y = 0$ ) is 100 G. The current sheet half-length is 0.2 of the vertical size of the lower half of the field structure—the part considered in the simulation. This vertical size is  $1.6 \times 10^9 \text{ cm}$ . The electrons are injected on the axis of symmetry, below the current sheet, over a vertical distance corresponding to the interval 0.64–0.8 of the vertical dimension. This reflects the vertical extent of the current sheet, as discussed in § 3.1. While in the no-convergence case, the geometry was assumed to be that of a flux rope with circular cross section, and a summation of the emission along the line of sight was made; in this case we assume uniform geometry in the direction perpendicular to the image-plane, and no such summation need be made to find the relative intensities in this image.

The coronal density value  $n = 3 \times 10^{10} \text{ cm}^{-3}$  is a reasonable value for a flare loop while the flare is in progress; however, early in the flare the loop is expected to have a lower density. Simulations made for a lower density, which represent the early part of the flare, are made in § 5.

The maps for the cases with and without field convergence are shown in Figure 5. In both cases, all electrons are injected at a single time, and the maps are integrals over the lifetime of all electrons in the distribution. This gives an image that is equivalent to that which would result in the steady state from the time-independent but continuous injection of a distribution with the same parameters.

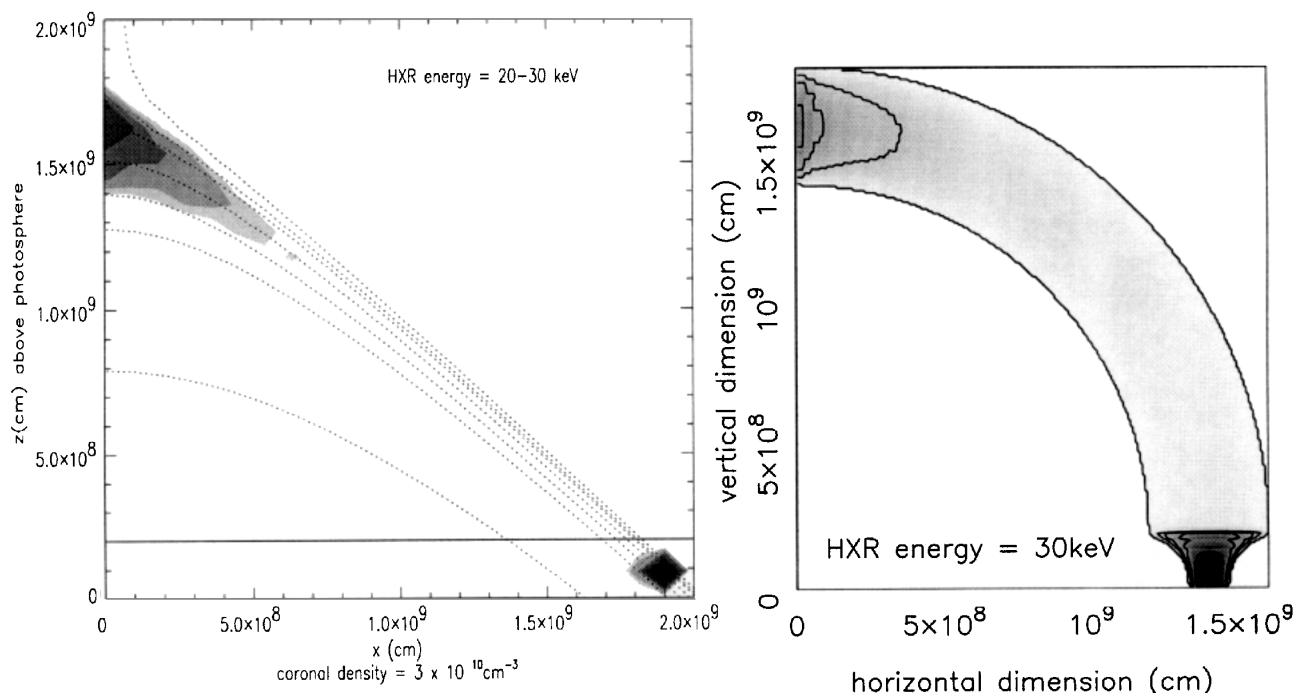


FIG. 5.—Calculated loop intensity maps; comparison of the looptop sources obtained with the two-field models. Note that in the right-hand panel, taken from Fletcher (1995), the photon energy given in fact refers to the upper energy of a 10 keV wide bin; i.e., this is the integrated emission in the 20–30 keV bin. Note that the gray scale is not consistent between the two images, but the plotted contours are, allowing comparison of the source sizes. All contours are relative to the highest counts in the image and are plotted at 12.5%, 17.5%, 25%, 34%, 50%, and 70%.

It can be seen that in the case of strong field convergence in the corona (Fig. 5, *left panel*) a looptop source exists and is larger and more intense at 20–30 keV than in the no-convergence case. This we attribute to the additional effect of particle trapping in the strongly convergent magnetic field at the top of the loop. For further comparison we show the maps produced at the higher energy of 40–50 keV. Recall that in the no-convergence case one problem was that the looptop source appeared larger at higher energy, in contradiction to the qualitative behavior of the observed source. It will be seen in Figure 6 that now this is no longer the case; the source is smaller and fainter at high energy than at low energy, in agreement with the observations.

To understand the variation of looptop source size with energy, it is necessary to consider the angular distribution of electrons generating the looptop source: those trapped by the strong magnetic convergence near the loop apex. The size of the looptop source at a given photon energy is determined by the distance, on average, of the mirror points of electrons of that energy and above. Low pitch-angle (trapped) electrons mirror at a greater distance than high pitch-angle electrons. The fact that the low-energy source is larger than the high-energy source is then indicative of a relatively larger population of low pitch-angle, low-energy, trapped electrons. This is indeed what is found when the angular distribution of electrons at a given energy is examined. The lower energy pitch-angle distribution is broader than the higher energy distribution. Both distributions are narrower than the  $\sin(\theta)$  distribution, which corresponds to the isotropic case. This can be seen in Figure 3.

It must be explained why the angular distributions have this form. The shape of the angular distribution is determined by two effects. The presence of the loss cone accounts for there being fewer low pitch-angle particles in the trapped distribution compared to the isotropic case, and

collisions tend to fill the loss cone gap in a way that depends on energy.

The loss cone is the region in velocity space with half angle  $\theta_0(S) = \arcsin [B(S)/B_{\max}]^{1/2}$ . In the complete absence of scattering, all particles at position  $S$  with pitch angles less than  $\theta_0(S)$  cannot be prevented by magnetic trapping from reaching the position at which  $B = B_{\max}$ , from where they are assumed to precipitate to the chromosphere and be lost. Those injected with angles greater than  $\theta_0$  would be trapped indefinitely at the looptop. The presence of scattering alters this. However, a loss cone distribution of some sort is maintained *unless* scattering is strong, a condition described by

$$\tau_{\mu\mu} \ll \tau_c = L_{\text{trap}}/v(1 - \cos \theta_0), \quad (6)$$

where the timescale for complete isotropization of the distribution is

$$\tau_{\mu\mu} = \frac{1}{D_{\mu\mu}} = \frac{m_e^2 v^3}{8\pi\Lambda ne^4}. \quad (7)$$

This is the timescale for a particle of speed  $v$  to undergo a  $90^\circ$  deflection. For the parameters of interest in these simulations, scattering is in general not strong. The particle speed at 30 keV is  $v = 10^{10}$  cm s $^{-1}$ . The maximum value of  $L_{\text{trap}}$  is the loop length in the corona,  $L = 2.2 \times 10^9$  cm; although, because of the nature of the field convergence, most of the trapping occurs near the loop apex. Halfway down the loop leg, the loss cone has widened to  $45^\circ$ . A value of  $L_{\text{trap}} \sim 10^9$  cm is possibly more representative. If  $L_{\text{trap}} = L = 2.2 \times 10^9$  cm, then  $\theta_0$  varies between  $\sim 15^\circ$  and  $30^\circ$ , depending on the  $y$ -value of the particle at injection (vertical positions between 0.8 and 0.64 in scaled units), and  $\tau_c \sim 1.6$ – $6.5$  s. If we take  $L_{\text{trap}} = 1.1 \times 10^9$  and calculate a new  $B_{\max}$  from this, then  $\theta_0$  varies between  $30^\circ$  and  $45^\circ$ , and  $L_{\text{trap}}/v(1 - \cos \theta_0) \sim 0.4$ – $0.8$  s. At a density of  $3 \times 10^{10}$

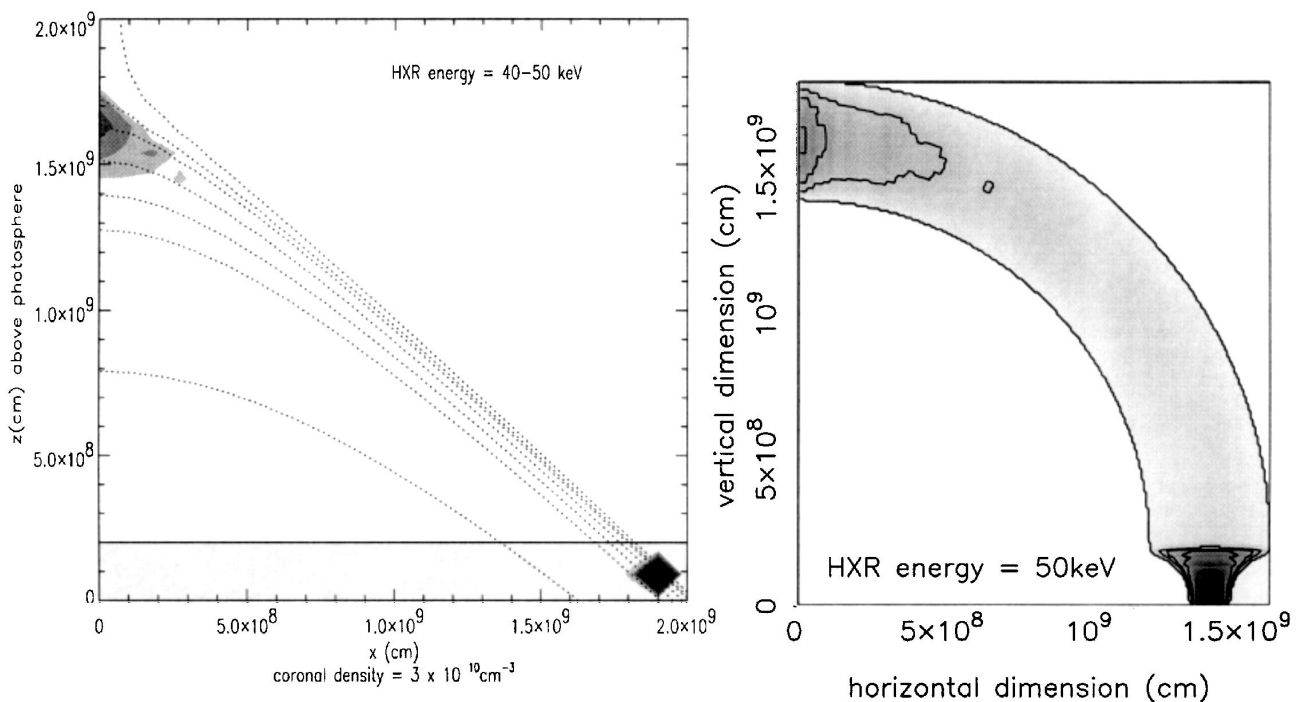


FIG. 6.—As in Fig. 5, but for emission in the interval 40–50 keV

$\text{cm}^{-3}$ , a particle speed of  $10^{10} \text{ cm s}^{-1}$  and  $\Lambda \sim 29$ ,  $\tau_{\mu\mu} = 0.7 \text{ s}$ , which means that scattering is only truly strong (e.g.,  $\tau_{\mu\mu} < 0.1\tau_c$ ) for a small fraction of the 30 keV population at this density. And bearing in mind that  $\tau_{\mu\mu}$  varies as  $v^3/n$  while  $\tau_c$  decreases as  $v$ , scattering cannot be considered strong for higher energy particles in lower density loops. We therefore expect that a loss cone will exist.

The presence of any degree of scattering allows particles near the loss cone boundary to be scattered into the loss cone, whence they precipitate on a transit timescale  $\tau_{\text{tr}} = L_{\text{trap}}/v\mu$ . (In principle, a particle can be scattered back out of the loss cone before precipitating, but any scattering to smaller pitch angles results in the ratio of  $\tau_{\mu\mu}$  to  $\tau_{\text{tr}}$  increasing, meaning that it becomes increasingly unlikely that a particle scattered to a lower pitch angle will be scattered again before leaving the trap.) The time taken for a particle to be scattered into the loss cone decreases with its angular displacement from the loss cone boundary, and the distribution will therefore be most rapidly depleted of particles (relative to an isotropic distribution) near the loss cone boundary. The angular distribution of trapped particles is thus narrower than an isotropic distribution, as is indeed observed in our simulations (Fig. 3).

The question remains why the trapped particle distribution is broader at lower particle energies. Were scattering not an energy-dependent process, the shape of the angular distribution at all energies would be the same, determined only by the input angular distribution and the size of the loss cone. The particle deficit near and in the loss cone at a particular energy must be filled by particles scattered down from higher energies. The rate at which this happens is strongly dependent on particle energy, with high-energy particles being collisionally degraded in energy at a lower rate than low-energy particles (the mean scattering expression indicates that  $dE/dt \sim 1/E^{1/2}$ ). The gap around the loss cone at low energies is thus filled in faster than that at high energies, resulting in a broader distribution at low energies. This, as we have already said, is consistent with a larger looptop source at low energies.

In the case of no magnetic trapping, presented in Fletcher (1995), the source size is determined solely by the effects of scattering on the particle distribution at different energies. The source is generated primarily by particles which, because of their high initial pitch angles, spend a large fraction of their radiating lifetimes orbiting the field at the top of the loop. The source size then reflects the parallel distance traveled from injection before collisions scatter particles to small pitch angles, at which point they free-stream to the chromosphere. Because of the smaller parallel collisional mean-free path of low-energy electrons, the source is smaller at low energies, contrary to observations.

The calculated spectra of the looptop and footpoint sources are shown in Figure 7. The total, angle-integrated HXR flux ( $\text{ergs cm}^{-1} \text{ s}^{-1} \text{ keV}^{-1}$ ) has been calculated assuming a total electron energy injection rate in the acceleration region of  $10^{10} \text{ ergs cm}^{-2} \text{ s}^{-1}$  and normalizing the simulation results to this. To calculate the total  $\text{ergs s}^{-1}$  from the sources, one should multiply by the expected perpendicular line-of-sight (LOS) depth of the loop structure. Thus if the LOS depth of the loop structure is  $10^9 \text{ cm}$ , then the looptop HXR flux is  $\sim 10^{20} \text{ ergs s}^{-1}$  at 20 keV, while the injection rate of electrons is  $\sim 2.56 \times 10^{27} \text{ ergs s}^{-1}$  (to get this total flux we have multiplied injection rate  $\times$  loop LOS depth  $\times$  length of current sheet along which electrons

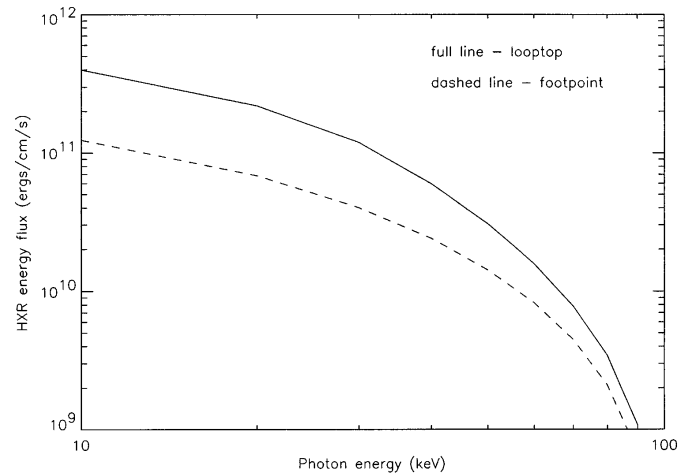


FIG. 7.—Spectra resulting from an injection of  $10^{10} \text{ ergs s}^{-1}$  total energy flux of electrons into the model, at a density of  $3 \times 10^{10} \text{ cm}^{-3}$  in the loop.

are injected). All of these numbers are reasonable for medium to large flares. The spectra show the characteristic that the looptop spectrum is softer than the footpoint spectrum (as the footpoint spectrum is a thick target spectrum, whereas the looptop spectrum, especially at higher energy, is a blend of thick and thin target effects). The looptop source, being larger (because of the field geometry), here generates a higher photon flux at Earth than the footpoint source; however, this is dependent on the loop geometry, density, and electron injection profile

##### 5. THE GENERATION OF A LOOPTOP HXR SOURCE IN A LOW-DENSITY LOOP

The looptop source is observed at the onset of the impulsive part of the flare, when, according to standard theory, flare evaporation has not yet filled the loop with high-density plasma. Theoretical hydrodynamic models of the response of the chromosphere to thick-target electron heating of the chromosphere (e.g., Nagai & Emslie 1984) indicate that it takes several tens of seconds to minutes (depending on the energy input rate) for chromospheric plasma to fill the loop, but the impulsive looptop source is visible from the beginning of the impulsive phase (after triggering of the HXT counters). In this section we also study the formation of looptop sources in low-density loops.

We choose a loop number density of  $4 \times 10^9 \text{ cm}^{-3}$ , about an order of magnitude lower than in the previous simulations and keep the loop length as before. The density is chosen to represent conditions in the impulsive loop, based on observational and theoretical arguments, as follows: It is reported in Tsuneta et al. (1997) that the SXR emission measure at the location of the HXR looptop source in the impulsive phase, is a few to 10% of the peak emission measure of the loop. From Masuda et al. (1995), this peak intensity is  $\sim 8 \times 10^{46} \text{ cm}^{-3} (\text{SXT pixel})^{-1}$ , so we take as an estimate a value at the looptop source of 5% of this or  $4 \times 10^{45} \text{ cm}^{-3} (\text{SXT pixel})^{-1}$ . One SXT pixel has an area at the Sun of  $(\sim 1800 \text{ km})^2$ , so the volume emission measure  $EM$  is  $\sim 1.2 \times 10^{29} \text{ cm}^{-5}$ . Assuming that the line-of-sight integration length  $L_{\text{int}}$  of SXT is approximately one coronal scale height,  $= 10^{10} \text{ cm}$ , the density  $= (EM/L)^{1/2} = 3.5 \times 10^9 \text{ cm}^{-3}$ .

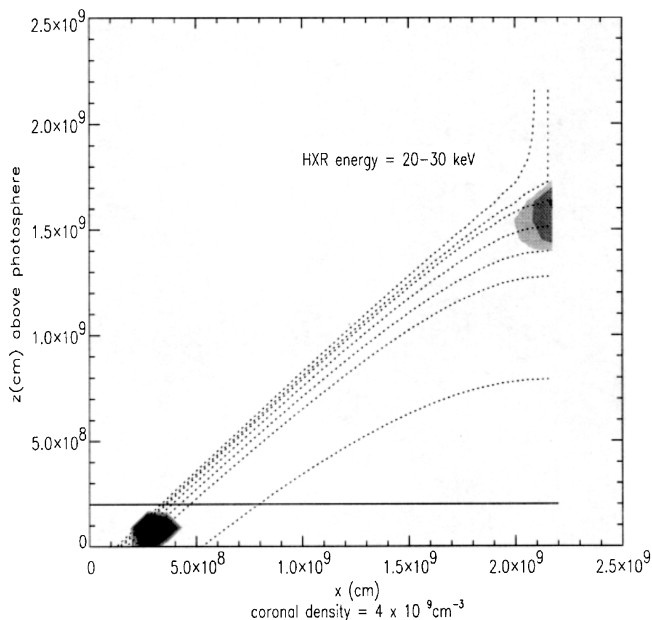


FIG. 8.—Calculated loop intensity map. Looptop source generated in a low-density loop ( $4 \times 10^9 \text{ cm}^{-3}$ ) by an injected electron distribution  $f(\mu) = \mu$ . Other parameters are as in previous simulations.

Alternatively, one can estimate the impulsive loop density using the scaling law for coronal loops

$$T_{\max} = 1400(PL)^{1/3} \quad (8)$$

(Rosner, Tucker, & Vaiana 1978; Craig, McClymont, & Underwood 1978), where  $T_{\max}$  is the temperature at the top of the loop (maximum loop temperature in a stable loop),  $P$  is the loop pressure, and  $L$  is the loop half-length. In these simulations, the loop length is  $2.4 \times 10^9 \text{ cm}$ , so assuming a (preflare) looptop temperature of  $\sim 2\text{--}3 \times 10^6 \text{ K}$ , we find  $n = 4.4\text{--}9.9 \times 10^9 \text{ cm}^{-3}$ . Our density of  $4 \times 10^9 \text{ cm}^{-3}$  is therefore a reasonable value.

The injected electron energy spectrum we keep as before, but from running test simulations with various angular input distributions, we have found that it is necessary to inject a somewhat broader distribution of electrons. The

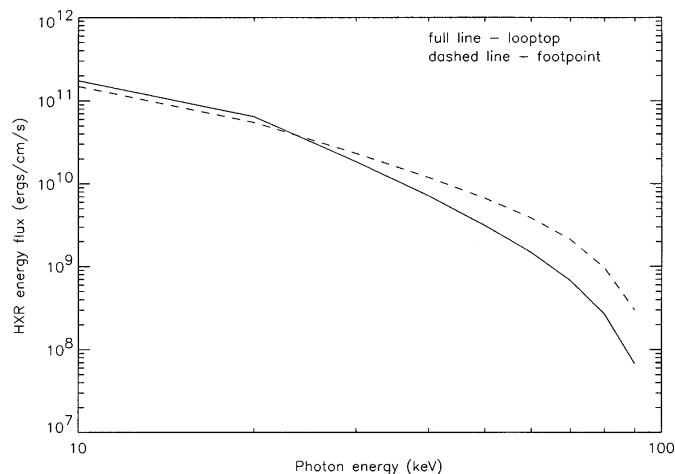


FIG. 9.—Spectra resulting from an injection of  $10^{10} \text{ ergs s}^{-1}$  total energy flux of electrons into the model, at a density of  $4 \times 10^9 \text{ cm}^{-3}$  in the loop.

reason for this is clear: a lower target density in the loop means that the relative looptop to footpoint emission is smaller, and the looptop is not visible unless we introduce an additional means to keep the beam particles at the looptop for longer. This we do by broadening the angular distribution so that electrons stay at the looptop for longer. The distribution used in the results presented here is  $f(\mu)d\mu = \mu d\mu$ , which, though broader than was previously used, is still beamed along the field direction.

The result of the simulation is shown in Figure 8, where it is apparent that a small looptop source is obtained. At higher energies the source is again smaller (although we do not show this result here). The HXR spectrum from this impulsive source is shown in Figure 9. Once again, it demonstrates a spectral steepening with increasing energy, although this time the looptop source has a lower intensity relative to the footpoint source because of its smaller size.

We have demonstrated in this section that it is possible to form a looptop source in a low-density loop with reasonable injection conditions. The changing density with time as the flare proceeds will constitute an interesting development for the transport and trapping simulation we use here.

## 6. LOCALIZED HEATING IN THE LOOP LEGS

In the 1992 January 13 flare analyzed by Masuda et al. (1995) and Tsuneta et al. (1997), a hot source ( $T \sim 15\text{--}20 \text{ MK}$ ) in SXT coincides with the impulsive HXR looptop source seen by HXT, while the peak in SXT emission measure is located distinctly below that. The emission measure of the hot SXT source is 4 orders of magnitude larger than that of the impulsive HXR looptop source, if one assumes thermal HXR emission.

As the flare progresses, the hot SXT source bifurcates, and the two-temperature maxima gradually move down the legs of the flare loop, while the impulsive HXR looptop source disappears and is later replaced by a more gradual HXR source with a softer spectrum, near the top of the SXR loop.

Furthermore, in the decay phase of the long-duration flare of 1992 February 21, Tsuneta (1996) found two temperature maxima flanking a cooler region at the top of a loop structure. The temperature distribution can be found in Tsuneta 1996 (that paper's Fig. 3, *top left panel*).

Tsuneta et al. (1997) and Tsuneta (1996) have attributed their observations to heating by standing shocks, which also confine the looptop plasma. In this section we demonstrate how it is possible to locally heat loop plasma at some distance from the reconnection sheet if proton beams are also present. Proton beams can generate hot spots at their mirroring positions, which may provide an alternative explanation for the observations summarized above.

When a particle is mirroring, its perpendicular velocity component increases at the expense of its parallel velocity component, so the distance traveled along the field per unit time decreases near the mirror point. Thus it spends a large fraction of its time near the mirror point, and we would expect to see a local maximum in the particle distribution function occurring at the mirror point.

However, this situation is complicated by the effect of scattering. Benz & Gold (1971) argued that in the presence of collisions, the mirror position of a particle moves as a function of time toward higher field regions, and the paths of individual particle in our simulations confirm this. Physically, because particles near the mirror point have large

perpendicular velocities, most collisions near the mirror point will tend to increase the parallel velocity component at the expense of the perpendicular component. So the position of the mirror point moves a little farther down each time particles approach it. Part of the reason that we find an extended HXR source generated by *electrons* is the movement of the mirror point: we see the time-integrated result. This source is also centered at the looptop, rather than displaced from it, because for electrons, pitch angle changes and energy loss occurs rapidly, and with (almost) the same timescale; the beam particles are confined to the looptop by both processes. But the situation is different for protons.

When a charged beam of electrons *or* protons enters an ionized target, the energy losses of the beam particles occur via interactions with the electrons in the target, whereas scattering occurs via interactions with the ions. For an electron beam, the timescale for pitch-angle change (defined by  $\mu/\dot{\mu}$ ) is almost the same as the energy loss timescale ( $E/\dot{E}$ ). However, for a proton beam, collisions with the target ions result in smaller deflections than for an electron beam, and the timescale for pitch-angle change for protons is longer than their loss timescale, by a factor 2 to infinity, depending on the pitch angles of the particles (with lower pitch angles giving a larger  $\mu/\dot{\mu}$ ). Although a proton beam is collisionally stopped after the same number of collisions as stops an electron beam of the same velocity, the virtual absence of scattering means that it on average travels a greater distance parallel to the field before being collisionally stopped. In addition, because of the lack of diffusion, the position of the mirror points of the protons is not smeared out to such an extent; the range in mirror positions in a given background density is determined chiefly by the initial proton energy distribution. The result of these properties of proton transport is that proton mirror points are concentrated quite well around a position displaced from the looptop. And since the protons are losing energy collisionally despite not undergoing collisional pitch-angle changes, they are heating the surrounding medium.

We shall say a little here about proton acceleration in this context. It is possible to accelerate both protons and electrons in a reconnecting current sheet (RCS) geometry such as we envisage in our model. As was shown by Speiser (1965), Martens (1988), and Martens & Young (1990), the presence in a RCS of a small field component perpendicular to the plane of the sheet results in the acceleration of protons and electrons to the same velocity in the sheet, which leaves the sides of the RCS as a neutral beam. Litvinenko (1996) introduced a third, longitudinal magnetic field component (in our model the component out of the  $x$ - $y$  plane), which has the role of magnetizing particles in the sheet, preventing them from leaving the RCS so rapidly and permitting acceleration to higher energies. The longitudinal field necessary to magnetize a particle species depends on the square root of the particle mass; therefore, it is possible to have a situation where the longitudinal field is high enough to magnetize the electrons in the RCS but not the protons, which are still ejected after half an orbit. Decreasing the strength of the longitudinal component changes the beam from an electron- to a proton-dominated one (in terms of the species carrying the bulk of the beam energy). The longitudinal field component, and thus the ratio of electron to proton energy flux, is a free parameter. It is interesting that, for the typical magnetic and electric field values given by Litvinenko (1996) for the RCS in the solar

flare case—i.e.,  $B_0 = 100$  G,  $B_{\text{long}} = 10$  G,  $B_{\perp} = 1$  G, and  $E_0 = 10$  V cm $^{-1}$ —a beam is created in which (assuming equal numbers of protons and electrons in the RCS) protons are the energy-carrying component, having energies in the range 0.1–1 MeV (electrons can be accelerated up to around 0.1 MeV). These are the typical energies adopted in the proton-transport simulation.

Proton transport is treated in the same way as electron transport, by following the evolution with a stochastic simulation. We inject a power-law distribution in number flux with spectral index 3 and cutoff at 0.5 MeV. The other parameters are as in § 4.1.

In Figure 10 we plot the Coulomb loss rate for protons as a function of position along the loop. The position of the maximum in the Coulomb loss rate is the position of the maximum of local heating and indicates where a temperature maximum would be located. Evidently this heating maximum, and thus the temperature maximum, is displaced from the injection position, unlike what occurs for an electron beam. The maximum is located at 15% of the distance from the end of the current sheet along the loop legs and is seen in time-dependent simulations to reach this location rapidly and be stable over the duration of the simulation (about 2 s). The simulations serve to show that the phenomenon of localized heating in the loop legs can take place, but we do not at this stage attempt to model the temperature distribution in any particular flare. The location of a heating maximum will be dependent on properties such as the initial pitch-angle distribution of the injected protons, the loop density distribution, and the magnetic field convergence.

What is the energy flux necessary in protons to achieve the observed temperature increase? Protons are injected over a finite time onto a field line, and the resulting pulse of particles must be able to transfer sufficient energy to heat the loop plasma from a preflare temperature of  $T_{\text{loop}} = 2\text{--}3 \times 10^6$  K to the observed ridge temperatures of  $T_{\text{ridge}} \sim 20$  MK over the lifetime of the pulse. Countering the heating,

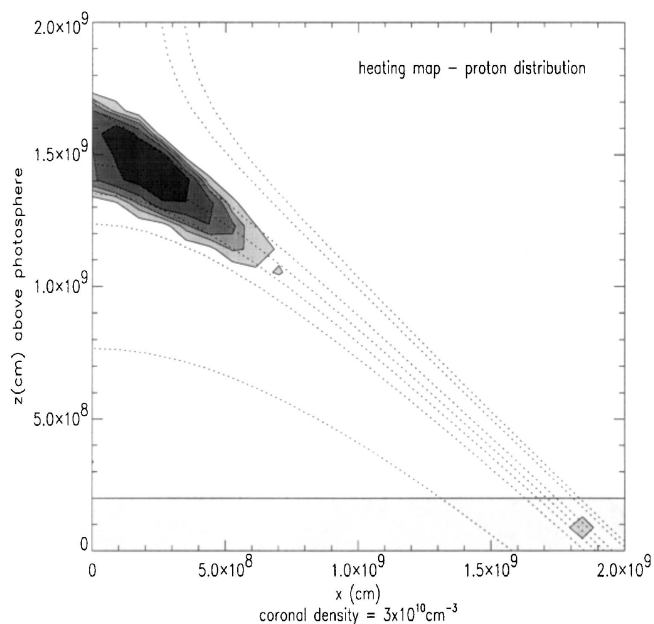


FIG. 10.—Coulomb loss rate for a proton power-law distribution,  $\delta = 3$ , low-energy cutoff at 0.5 MeV, in an ambient loop density of  $3 \times 10^{10}$  cm $^{-3}$ .

cooling of the high-temperature ridges will also take place, through conduction and radiation.

The timescale for conductive losses is given by

$$\tau_{\text{cond}} = \frac{3n_{\text{ridge}} k_B T_{\text{ridge}} (\Delta l)^2}{\kappa_0 T_{\text{ridge}}^{5/2} (T_{\text{ridge}} - T_{\text{loop}})}. \quad (9)$$

The Spitzer thermal conductivity  $\kappa_0 = 1.2 \times 10^{-6}$  ergs  $\text{s}^{-1} \text{cm}^{-1} T^{-3.5}$ . We shall use the observed values of the loop parameters from Tsuneta et al. (1997) for the January 13 flare in this calculation. The lengthscale  $\Delta l$  between maximum and minimum temperature (i.e., looptop) regions is  $\Delta l \sim 2 \times 10^4$  km (along curved field lines). The loop density at the ridge position is  $n_{\text{ridge}} = 1.5 \times 10^{10} \text{cm}^{-3}$ . The conductive cooling timescale is therefore  $\tau_{\text{cond}} \sim 13$  s. (Nota bene, if we insert the values used in our numerical calculations,  $n = 3 \times 10^{10} \text{cm}^{-3}$  and  $\Delta l \sim 3 \times 10^3$  km, we find  $\tau_{\text{cond}}$  to be shorter,  $\sim 1$  s, because of the smaller  $\Delta l$ ; however, as mentioned above, the position of the heating maximum can be varied by judicious choice of the loop density, the form of the field, and the injected proton distribution.)

The radiative loss timescale is

$$\tau_{\text{rad}} = \frac{3k_B T_{\text{ridge}}}{\Lambda_{\text{rad}}(T_{\text{ridge}})n_{\text{ridge}}}, \quad (10)$$

where  $\Lambda_{\text{rad}}$ , the radiative loss function, is given by  $\Lambda_{\text{rad}} \sim 6 \times 10^{-20} T^{-0.5}$  in the temperature regime of interest (see Tsuneta et al. 1997). Thus, using  $T_{\text{ridge}} = 20$  MK, and other parameters as above, gives  $\tau_{\text{rad}} \sim 4.0 \times 10^4$  s, far longer than any other timescales of interest.

We calculate below the local density, and thereafter the flux in protons, necessary to heat the ridges to the observed temperatures. In our model, the duration of the acceleration pulse of particles onto any given magnetic field line is  $\tau_{\text{inj}} \sim 2$  s, i.e., the time spent by a field line in the current sheet. Because of trapping and mirroring, a particle can remain on a field line for a longer time; however, to estimate the maximum beam flux necessary to heat the ridges, we assume that protons have only 2 s in which to deliver energy (by collisional losses) to the surrounding plasma and raise its temperature to 20 MK. The situation can be expressed, in terms of energy change per  $\text{cm}^3 \text{s}^{-1}$ , as follows:

$$n_b \frac{dE_{b,p}}{dt} = nk_b \left[ \frac{(T_{\text{ridge}} - T_{\text{loop}})}{\tau_{\text{inj}}} - \frac{T_{\text{ridge}}}{\tau_{\text{cond}}} \right]. \quad (11)$$

We can thus calculate the local beam density  $n_b$  necessary to heat the plasma. The rate  $dE_{b,p}/dt$  is the Coulomb loss rate for protons, from Emslie (1978). Putting in values derived from observed quantities and using  $\tau_{\text{inj}} \sim 2$  s gives  $n_b \sim 5 \times 10^7 \text{cm}^{-3}$  (assuming a proton energy at injection of 1 MeV and corresponding to a velocity at the mirroring position of  $10^9 \text{cm s}^{-1}$ ; see eq. [12]) at the site of local heating maximum. The beam density will be higher here at the heating maximum than at injection, and the density at a loop position  $S$  can be related to that at injection by considering continuity of proton number in the loop; i.e.,  $n_b(S)v_p(S)\mu_p(S)A(S) = n_b(0)v_b(0)\mu_p(0)A(0)$ , where  $A$  is the loop cross-sectional area, and  $v_b$ ,  $\mu_p$  are the beam particle velocity and pitch angle. Variation in  $v_b$  is caused by collisional losses, and  $\mu_b$  varies principally because of field con-

vergence. From Emslie (1978),

$$\frac{v_b(S)}{v_b(0)} = \left[ 1 - 2\lambda \left( \frac{m_p}{m_e} \right) \frac{2\pi e^4 N(S)}{\mu(0)E_{b,p}(0)^2} \right]^{1/2}. \quad (12)$$

A 1 MeV proton has to traverse a column depth  $N(S) \sim 4 \times 10^{19} \text{cm}^{-2}$  from injection to reach the mirroring point (using an average value for the loop density of  $2 \times 10^{10} \text{cm}^{-3}$  for the region between the looptop, where the observed density is  $3 \times 10^{10} \text{cm}^{-3}$ , and the heating positions, where it is  $1.5 \times 10^{10} \text{cm}^{-3}$ ). Thus  $v_b(S)/v_b(0) = 0.7$  at the mirror point [assuming  $\mu_b(0) = 1$ ]. In the observation, the ridge occurs around halfway down the loop legs. The value of  $A(0)/A(S)$  at halfway down the loop structure is a factor of a few in our field model, say  $A(0)/A(S) \sim 2$ . The ratio  $\mu_b(S)/\mu_b(0)$  is inevitably less than 1 because of mirroring; therefore,  $n_b(0)/n_b(S) < 0.35$ , and the beam density at injection  $n_b(0) < 1.8 \times 10^7 \text{cm}^{-3}$ . Assuming again that protons are injected with an energy of 1 MeV, the injected energy flux is  $< 4 \times 10^{10} \text{ergs cm}^{-2} \text{s}^{-1}$  and probably considerably less, given the fact that we have not considered the pitch-angle factor and have taken the worst case of  $\mu = 1$  at injection. This injected energy flux is quite acceptable for typical flares. Further, the hydrodynamic ram pressure presented by the beam at injection is considerably less than the thermal pressures measured in the loop by Tsuneta et al. (1997).

The injection pulse onto any given field line lasts for 1–2 s (this being the time spent by a field line in the current sheet) and localized heating can occur, at most, for the trapping time of protons in the loop, which at these densities is of the order of 10 s [ $L/(1 - \cos \theta_0)v$ ], less than or of the order of the thermal conduction time. During heating, energy is transferred rapidly from the beam protons to background electrons, which are then heated to the 20 MK temperatures observed. A conduction front propagates along the field toward the looptop on the conduction timescale; however, before it reaches the looptop, injection onto a single field line is switched off, and heating decays away before a uniform temperature distribution due to conduction can be established between the temperature maximum regions and the apex of a given reconnected field line. One would thus expect a temperature minimum at the top of recently reconnected field lines.

Proton beams are themselves capable of producing X-rays by bremsstrahlung, but the energy necessary for the production of an X-ray photon of energy  $\epsilon$  is typically  $E = (m_p/m_e)\epsilon$ , meaning that the protons we consider are not of high enough energy to generate keV HXR's. Similarly, electron beams are capable of localized heating, which in the loop would occur cospatially with the looptop hard X-ray source. How much of a difference would this make to the proton-generated ridges? First of all, there is good reason (see below) for expecting that either proton/neutral or electron beams will be present, but not both at the same time. Yet, should strong electron and proton beams with the parameters we have used in this paper both be present simultaneously, heat input by protons would still dominate. The rate of collisional energy loss locally depends on  $n_{b,i}/v_{b,i}$ , where  $i$  designates either electrons or protons and is thus determined by the injected particle distribution functions. As we are dealing with protons of energy  $E_p \sim 1$  MeV and  $E_e \sim 30$  keV, the heating rate by a single electron will generally be smaller than that by a single proton, by a factor

of  $\sim 10$ , because of higher electron velocities. Moreover, the local density of trapped protons will be higher than that of trapped electrons, assuming that the densities at injection are equal (which is reasonable, if there are equal densities in the current sheet, and implies an energy flux in 1 MeV protons 5 times higher than that in 30 keV electrons). This is because protons of  $\sim 1$  MeV are in the weak-scattering regime, and their loss time, determined by the Coulomb diffusion coefficient for protons, is  $\sim 5$  s (at a density of  $3 \times 10^{10} \text{ cm}^{-3}$ ), whereas the electron loss time is  $\sim 1$  s. Therefore not only is the heating per proton higher in the loop region than per electron, there are also more protons trapped. Additional heating due to trapped electrons would therefore not make a significant difference to the overall heating pattern.

There is reason to believe that proton beams do not occur simultaneously with strong electron beams, but in the form of neutral beams, in which case the proton component is unaffected by the evolution of the electron component (because of the protons' far higher momentum). Nonetheless, should there be both strong electron and proton beams simultaneously, we argue that they can form independent distributions with the background plasma, providing local charge neutralization where necessary. This assumption is necessary for the test particle method used; whether considering a single or a multiple species beam, it is not computationally possible to account for the beam's interaction with itself, and one must deal with timescales greater than that on which the background electrons can adjust to prevent the buildup of large potentials due to charge separation. Physically, this is a reasonable assumption to make. Van den Oord (1990) argues that electrostatic charge neutralization of a beam by the background plasma occurs on the collisional timescale for the background particles with themselves,  $\tau_{\text{coll}} = 0.83 T^{3/2} / n_{10} \text{ } \Lambda \text{ s}$ . For a background density of  $3 \times 10^{10} \text{ cm}^{-3}$  and a loop temperature  $T$  before heating of  $2\text{--}3 \times 10^6 \text{ K}$ , the neutralization timescale is thus 1–1.8 milliseconds and an order of magnitude higher for a background density of  $3 \times 10^9 \text{ cm}^{-3}$ , which is also the timescale on which transient adjustments of the background plasma are damped. This timescale is several orders of magnitude longer than the smallest possible acceleration timescales found in the Litvinenko (1996) model, meaning that, although the background plasma cannot readjust in the case of these extremely short (submillisecond) impulsive variations, variations on timescales greater than a few milliseconds should be charge-neutralized; e.g., for 30 keV electrons this corresponds to a maximum propagation (free-streaming) distance of  $> 1\text{--}2 \times 10^7 \text{ cm}$  in the higher density case. So, should it be necessary, we can assume that structures on size scales greater than this evolve without self-interaction of the beams being important.

However, there are observational as well as theoretical reasons for believing that strong electron and proton beams do not exist simultaneously in the flare. In the "Masuda" event, the disappearance of the looptop HXR source and the diminution to preflare levels of the total HXR flux (presumably due primarily to electron bremsstrahlung in the chromosphere), which peaks between 17.26 UT and 17.30 UT, indicates that strong electron beams are no longer present. The reduction of the HXR emission is accompanied by the bifurcation of the temperature structure, which nonetheless remains on the (reconnecting) field-lines outside the SXR-emitting loop. All of this might argue

for a transition from an electron beam- to a proton beam-dominated phase of the flare.

In an electron-dominated phase of the flare, one would expect to see a heated region at the top of the loop, coincident with the looptop HXR source, rather than in the legs. This would be the case if the electron beam carries the bulk of the energy and protons are accelerated to energies too low to carry them very far from the point of injection, as would occur in the Litvinenko RCS model if the longitudinal field component is high enough to magnetize electrons but not protons. In the "Masuda" event, the impulsive HXR looptop source is indeed coincident with a heated region at the looptop. The bifurcation of the heated region and the disappearance of the HXR emission can be elegantly explained by a change from electrons to protons as the energy-carrying species, plus an increase in the mean energy of the protons.

Within the context of the Litvinenko acceleration model, the change from an electron- to a proton/neutral-dominated flare corresponds to a decrease with time in the relative strength of the longitudinal magnetic field component in the RCS. Further, assuming that the longitudinal component is never high enough to magnetize protons, then an increase in proton energy corresponds to an increase in the ratio of the electric to perpendicular magnetic fields. It is well established observationally (Martin & McAllister 1996) that, as the current sheet rises, the shear of newly formed postflare loops decreases, and thus the ratio of the longitudinal field component to the component in the plane does indeed decrease with time. We therefore volunteer that in this event we are seeing the slow magnetic evolution of the flaring region reflected in the evolution of the observational signatures generated by accelerated particles. However, it is evident that more complex models, taking into account the changes in field structure and chromospheric evaporation, must be constructed to fully explore this exciting possibility.

## 7. DISCUSSION AND CONCLUSIONS

With the use of numerical simulations, we have demonstrated that a looptop source will arise in a convergent magnetic field geometry as a result of particle trapping and scattering. We have used a Syrovatskii current sheet field geometry (Syrovatskii 1971) and injected particles along the field lines leading from the current sheet into the loop. We have made a comparison with the work of Fletcher (1995), where no coronal magnetic field convergence was included, and found that a more intense looptop source can be generated than was previously possible for otherwise identical conditions. Further, we find that high-energy HXR sources are smaller, as observed by HXT (e.g., Masuda et al. 1995), but in contradiction to the no-convergence model (Fletcher 1995), which did not show this behavior. The source size is determined by the angular distribution of electrons trapped in the looptop and can be explained as a consequence of the presence of a loss cone distribution in the looptop, modified by the effect of a moderate level of energy-dependent particle scattering. Such a dependence of HXR looptop source size on energy may provide indirect evidence for a magnetic trap at the apex of flare loops.

We have also studied the case of a lower density loop, which might better emulate the conditions in the early impulsive phase of a flare. We find that with reasonable injection parameters a looptop source can also be generated at observable levels in a low-density loop, which was not

possible in the absence of coronal field convergence and is again the direct result of electron trapping by magnetic field convergence

The HXR emission from the looptop and the footpoints occurs on a timescale shorter than or comparable to the time a fieldline spends in the sheet. Hence it follows from our model that the looptop HXR source marks the location of the reconnecting current sheet, in contrast to the model of Masuda et al. (1995). Our model thus naturally accounts for the observation that the HXR looptops are usually located above the top of the SXR postflare loops, because the filling of these SXR loops by chromospheric evaporation takes tens of seconds to minutes, at which time the reconnected field lines have exited the sheet from the bottom.

It is appropriate at this point to pay some attention to the long-standing problem of the interpretation of the “Masuda” event in terms of a rising reconnection region. In such a model the rising reconnection region activates parts of the field that are more and more widely separated at the footpoints, and they are reconnected into successively larger loops. Given that the generation of footpoint HXR emission by electron beams follows reconnection and acceleration very rapidly but the lighting up of the SXR loop by evaporation takes some time, the HXR footpoints should lie outside the SXR loop. However, in the “Masuda” event and in a number of others (Masuda et al. 1997) the L, M1, and M2 HXR footpoints are found to lie within the SXR loops, (although this is not the case in seven of the 11 cases these authors examined). Moreover, in the left-hand footpoint of the “Masuda” event, successively higher energy footpoints are more displaced to the inside. The same effect is seen in the 1992 October 4 flare shown in Fig. 2.8 of Masuda (1994) for the left-hand side footpoint; there is an offset between the L and M1 bands, and both have an offset from the SXR footpoint.

These events might find an explanation in the following way: The bulk of the emission at the footpoints is not generated where the beam enters the chromosphere, but some column depth thereafter, the value being dependent on the energy of photons. For example, in their thick-target, mean-scattering calculations, Brown & McClymont (1975) found that the maximum emission rate of 25 keV photons for a beam with a power-law index  $\delta = 3$  occurs at a column depth of  $2 \times 10^{21} \text{ cm}^{-2}$ . Higher energy photons are generated primarily at larger column depths. Therefore, if the chromospheric part of the magnetic field that guides the beam particles is not vertical but bent inward, toward the vertical axis of the loop, the HXR emission at this optimum column depth will also be offset inward. Furthermore, the

higher the photon energy, the more pronounced this effect will be as the optimum column depth increases. To achieve a significant offset, however, the bend from the vertical must be significant; otherwise, the rapidly increasing density in the chromosphere will mean that the column depth will not translate into a very large physical depth, which, in turn, with only a small deviation of the field from vertical would appear only as a small horizontal offset.

It is reasonable to expect that in some flares the chromospheric field will indeed deviate significantly from the local vertical, and it should be possible to test which one, on the disk. In very young and fragmented activity complexes, where flares tend to occur, polarity inversion lines (PILs) abound. By definition, the LOS component of the magnetic field is zero near a PIL; therefore, the field is locally near-horizontal, often nearly parallel to the PIL, because of the large shear. In flares occurring over a PIL, an inward offset of HXR footpoints with respect to SXR loops could be expected. Such a correlation could be tested by examining coaligned HXT and SXT images and SOHO SOI/MDI magnetograms.

For example, in the case of the “Masuda” event, the offset in the M1 channel is of the order of 2–3 SXR pixels, or  $\sim 4000 \text{ km}$ . If this is to be explained by beam penetration effects in a tilted magnetic field, the density should not get much above  $\sim 2 \times 10^{21} \text{ cm}^{-3}/4 \times 10^8 \text{ cm} = 5 \times 10^{12} \text{ cm}^{-3}$ . In a chromosphere with exponentially increasing density, matched to a preflare loop density of  $4 \times 10^9 \text{ cm}^{-3}$ , this value is reached at 800 km below the top of the chromosphere. The angle of the magnetic flux tube below the chromosphere must therefore be  $< \tan^{-1} (400/8000) = 11^\circ$  to the horizontal.

We have in addition investigated the generation of the high-temperature “ridges” as observed in the “Masuda” flare and reported by Tsuneta et al. (1997). We find that the action of proton mirroring in the converging magnetic field together with the reduced effect of Coulomb collisions on protons, as compared to electrons, leads to the formation of temperature maxima, displaced from the injection point toward the footpoints. Such results are phenomenologically in good agreement with gradual phase observations with SXT and may provide interesting insights for relating the magnetic development of the flare with particle-generated signatures.

In conclusion, it appears that the model proposed elegantly reproduces many of the observed characteristics of the gradual and impulsive looptop HXR source.

We thank our anonymous referee for insightful comments, which have significantly improved this paper.

#### REFERENCES

- Alexander, D., & Metcalf, T. R. 1997, *ApJ*, 489, 442  
 Benz, A. O., & Gold, T. 1971, *Sol. Phys.*, 21, 157  
 Brown, J. C. 1972, *Sol. Phys.*, 26, 441  
 Brown, J. C., & McClymont, A. N. 1975, *Sol. Phys.*, 41, 135  
 Craig, I. J. D., McClymont, A. N., & Underwood, J. H. 1978, *A&A*, 70, 1  
 Doschek, G. 1994, in *Proc. Kofu Symp., A New Look at the Sun with Emphasis on Advanced Observations of Coronal Dynamics and Flares*, ed. S. Enome & T. Hirayama, NRO Report (Nobeyama Japan), 360  
 Elwert, G., & Haug, E. 1972, *Sol. Phys.*, 20, 413  
 Emslie, A. G. 1978, *ApJ*, 224, 241  
 Fletcher, L. 1995, *A&A*, 303, L9  
 ———. 1996, *A&A*, 310, 661  
 Haug, E. 1997, *A&A*, 326, 417  
 Holman, G. 1996, *BAAS*, 28, 939  
 Hudson, H. S., & Ryan, J. M. 1995, *ARA&A*, 33, 239  
 Kosugi, T., et al. 1991, *Sol. Phys.*, 136, 17  
 Litvinenko, Y. E. 1996, *ApJ*, 462, 997  
 MacKinnon, A. L., & Craig, I. J. D. 1991, *A&A*, 251, 693  
 Martens, P. C. H. 1988, *ApJ*, 330, L131  
 Martens, P. C. H., & Kuin, N. P. M. 1989, *Sol. Phys.*, 122, 263  
 Martens, P. C. H., & Young, A. 1990, *ApJS*, 73, 333  
 Martin, S. F., & McAllister, A. H. 1996, in *IAU Colloq. 153, Magnetohydrodynamic Phenomena in the Solar Atmosphere, Prototypes of Stellar Magnetic Activity*, ed. Y. Uchida, H. S. Hudson, & T. Kosugi (Dordrecht: Kluwer), 497  
 Masuda, S. 1994, Ph.D. thesis, Univ. Tokyo  
 Masuda, S., Kosugi, T., Hara, H., Sakao, T., Shibata, K., & Tsuneta, S. 1995, *PASJ*, 47, 677  
 Masuda, S., Kosugi, T., Hara, H., Tsuneta, S., & Ogawara, Y. 1994, *Nature* 371, 495  
 Masuda, S., Sakao, T., Kosugi, T., & Sato, J. 1997, *BAAS (Proc. SPD meeting)*, 29, 892

- Nagai, F., & Emslie, A. G. 1984, *ApJ*, 279, 896  
Petrosian, V. 1973, *ApJ*, 186, 291  
Priest, E. R. 1981, in *Solar Flare Magnetohydrodynamics*, ed. E. R. Priest (New York: Gordon and Breach), chap. 3  
Rosner, R., Tucker, W. M., & Vaiana, G. S. 1978, *ApJ*, 220, 643  
Simnett, G. M., & Strong, K. T. 1984, *ApJ*, 284, 839  
Speiser, T. W. 1965, *J. Geophys. Res.*, 70, 4219  
Syrovatskii, S. I. 1971, *Soviet Phys.-JETP Lett.*, 33, 933  
Takakura, T., Tanaka, K., Nitta, N., Kai, K., & Ohki, K. 1987, *Sol. Phys.*, 107, 109  
Tsuneta, S., Hara, H., Shimizu, T., Acton, L. A., Strong, K. T., Hudson, H. S., & Ogawara, Y. 1992, *PASJ*, 44, L63  
Tsuneta, S. 1996, *ApJ*, 456, 840  
Tsuneta, S., Masuda, S., Kosugi, T., & Sato, J. 1997, *ApJ*, 478, 787  
van den Oord, G. H. J. 1990, *A&A*, 234, 496  
Wheatland, M. S., & Melrose, D. B. 1995, *Sol. Phys.*, 158, 283